View metadata, citation and similar papers at core.ac.uk

brought to you by CORE

provided by University of Central Florida (UCF): STARS (Showcase of Text, Archives, Research &...

University of Central Florida

STARS

Faculty Bibliography 2000s

Faculty Bibliography

1-1-2005

Comprehensive modeling of near-field nano-patterning

Raymond C. Rumpf
University of Central Florida

Eric G. Johnson
University of Central Florida

Find similar works at: https://stars.library.ucf.edu/facultybib2000
University of Central Florida Libraries http://library.ucf.edu

This Article is brought to you for free and open access by the Faculty Bibliography at STARS. It has been accepted for inclusion in Faculty Bibliography 2000s by an authorized administrator of STARS. For more information, please contact STARS@ucf.edu.

Recommended Citation

Rumpf, Raymond C. and Johnson, Eric G., "Comprehensive modeling of near-field nano-patterning" (2005). *Faculty Bibliography 2000s*. 5621.
https://stars.library.ucf.edu/facultybib2000/5621

Comprehensive modeling of near-field nano-patterning

Raymond C. Rumpf, Eric G. Johnson

College of Optics/CREOL&FPCE, University of Central Florida, Orlando, Florida 32816
eric@creol.ucf.edu

http://mpl.optics.ucf.edu/

Abstract: Near-field nano-patterning greatly simplifies holographic lithography, but deformations in formed structures are potentially severe. A fast and efficient comprehensive model was developed to predict geometry more rigorously. Numerical results show simple intensity-threshold methods do not accurately predict shape or optical behavior. By modeling sources with partial coherence, unpolarized light, and an angular spectrum, it is shown that standard UV lamps can be used to form 3D structures.

©2005 Optical Society of America

OCIS Codes: (000.3860) Mathematical methods in physics; (000.4430) Numerical approximation and analysis; (050.0050) Diffraction and gratings; (090.0090) Holography; (130.0130) Integrated optics; (160.5470) Polymers; (220.3740) Lithography; (220.4000) Microstructure fabrication; (230.0230) Optical devices; (350.3950) Micro-optics; (999.9999) Photonic crystals; (999.9999) Numerical modeling.

References and Links

1. John D. Joannopoulos, Robert D. Meade, Joshua N. Winn, *Photonic Crystals*, (Princeton University Press, Princeton, New Jersy, 1995).
2. Y. V. Miklyaev, D. C. Meisel, A. Blanco, G. Freymann, K. Busch, W. Kock, C. Enkrich, M. Deubel, M. Wegener, "Three-dimensional face-centered-cubic photonic crystal templates by laser holography: fabrication, optical characterization, and band-structure calculations," Appl. Phys. Lett. **82,** 1284-1286 (2003).
3. L. Z. Cai, X. L. Yang, Y. R. Wang, "Formation of three-dimensional periodic microstructures by interference of four noncoplanar beams," J. Opt. Soc. Am. A **19,** 2238-2244 (2002).
4. L. Z. Cai, X. L. Yang, Y. R. Wang, "All fourteen Bravais lattices can be formed by interference of four noncoplanar beams," Opt. Lett. **27(11),** 900-902 (2002).
5. S. Jeon, G. Wiederrecht, J. A. Rogers, "Photonic systems formed by proximity field nanopatterning," in *Proceedings of SPIE Micromachining Technology for Micro-Optics and Nano-Optics III* **5720**, E. G. Johnson, ed. (SPIE, Bellingham, WA, 2005), pp. 187-195.
6. R. C. Rumpf, E. G. Johnson, "Fully three-dimensional modeling of the fabrication and behavior of photonic crystals formed by holographic lithography," J. Opt. Soc. Am. A **21,** 1703-1713 (2004).
7. R. C. Rumpf, E. G. Johnson, "Modeling the formation of photonic crystals by holographic lithography," in *Proceedings of SPIE Micromachining Technology for Micro-Optics and Nano-Optics III* **5720**, E. G. Johnson, ed. (SPIE, Bellingham, WA, 2005), pp. 18-26.
8. S. Robertson, E. Pavelchek, W. Hoppe, R. Wildfeuer, "Improved notch model for resist dissolution in lithography simulation," in *Proceedings of SPIE Advances in Resist Technology and Processing XVIII* **4345**, F. M. Houlihan, ed., 912-920 (2001).
9. M. G. Moharam, E. B. Grann, D. A. Pommet, T. K. Gaylord, "Formulation for stable and efficient implementation of the rigorous coupled-wave analysis of binary gratings," J. Opt. Soc. Am. A **12,** 1068-1076 (1995).
10. M. G. Moharam, D. A. Pommet, E. B. Grann, T. K. Gaylord, "Stable implementation of the rigorous coupled-wave analysis for surface-relief gratings: enhanced transmittance matrix approach," J. Opt. Soc. Am. A **12,** 1077-1086 (1995).
11. F. H. Dill, "Positive Optical Lithography," *Conf. IEEE International Solid-State Circuits*, 54-55 (1975).
12. Y. Shacham-Diamond, "Modeling of Novolak-Based Positive Photoresist Exposed to KrF Excimer Laser UV Radiation at 248 nm," *IEEE Trans. Semiconductor Manufacturing* **3(2),** 37-44 (1990).
13. Z. Ling, K. Lian, L. Jian, "Improved patterning quality of SU-8 microstructures by optimizing the exposure parameters," in *Proceedings of SPIE Advances in Resist Technology and Processing XVII*, 1019-1027 (2000).
14. J. A. Sethian, *Level Set Methods and Fast Marching Methods: Evolving interfaces in computational geometry, fluid mechanics, computer vision, and materials science*, (Cambridge University Press, New York, New York, 1999).

#7975 - $15.00 USD Received 29 June 2005; revised 1 August 2005; accepted 30 August 2005
(C) 2005 OSA

15. "The SU-8 photoresist for MEMS," http://aveclafaux.freeservers.com/SU-8.html.
16. EXFO Application Note 088, "High Power UV Light Sources," (EXFO, 2005) http://www.exfo-uv.com/App_Notes/High_Power_UV_Light_Sources.pdf.
17. MicroChem Product Data Sheet for SU-8 2007, "NANO™ SU-8 2000 Negative Tone Photoresist Formulations 2002-2025," (MicroChem, 2005), http://www.microchem.com/.

1. Introduction

Photonic crystals (PC), or photonic bandgap materials, are structures with sub-wavelength periodic material properties that can produce sharp electromagnetic resonances [1]. These structures provide a means of controlling and engineering bulk optical properties of materials. Many novel and useful phenomena have been observed that promise significant impact on future photonic systems such as forbidden transmission and anomalous dispersive properties.

Holographic lithography [2-4], or interference lithography, is a promising method of fabrication. In a single process step, high-resolution photoresist materials like Epon® SU-8 can be exposed with UV, electron beam, or x-ray radiation to form photonic crystals. It has been shown that all fourteen Bravais lattices symmetries can be realized by interfering just four noncoplanar beams [4]. The method and associated materials are flexible and easily integrated with other devices. Near-perfect periodicity can be achieved because no alignment steps are necessary. Holographic lithography, however, can be very sensitive to mechanical vibration and require high beam coherence. This leads to rather sophisticated laboratory setups to implement the method.

Near-field nano-patterning (NFNP) is a form of holographic lithography that greatly simplifies the process [5]. A high-resolution phase mask is placed in close proximity or in direct contact with photoresist. The phase mask diffracts incident light, forming the desired hologram within the photoresist. This method is more immune to mechanical vibration because masks can be rigidly fixed in position with the resist. Standard ultraviolet (UV) lamps can be used as sources because required coherence length is only several microns. Figure 1 illustrates this method.

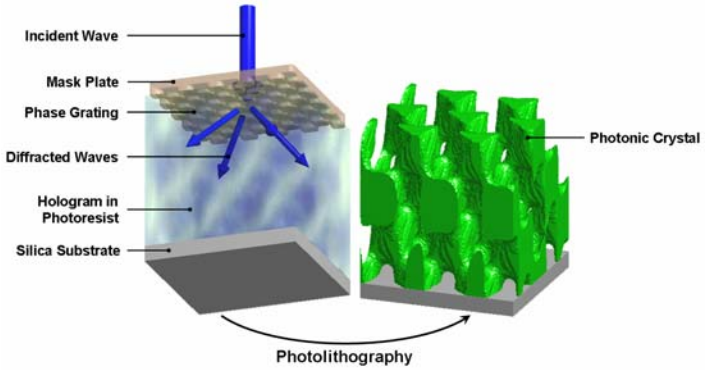

Fig. 1. (850 kb) Movie of near-field nano-patterning process.

When forming structures at the nano-scale, distorting artifacts of fabrication are quite pronounced. To predict geometry, it is important to consider the entire fabrication process because even small deformations of the lattice can have dramatic impact on optical behavior. In previous work, holographic lithography was comprehensively modeled for 3D photonic crystals [6,7]. Optical absorption during exposure was shown to lead to chirped lattices. The effect was quantified by comparing image contrast to solubility properties of the photoresist. Reflections and standing waves were shown to cause lattice distortions by effectively adding extra beams to the hologram. Acid diffusion during post exposure bake was shown to blur exposed images, but contribute to lattice connectivity. It was shown that conventional intensity threshold schemes lead to considerably less accurate predictions of optical behavior

#7975 - $15.00 USD Received 29 June 2005; revised 1 August 2005; accepted 30 August 2005
(C) 2005 OSA

because these methods fail to adequately predict geometry. Simulated results compared remarkably well to experimental.

This paper builds on this initial work in several regards. First, a more efficient comprehensive model was developed to simulate NFNP. A numerical example is presented where results are compared to intensity thresholding. Second, it is shown that illumination from standard UV lamps can be used to form 3D structures using NFNP. Impact of partial coherence, unpolarized light, and unfiltered light are demonstrated through simulation. Third, angular spectrum of source illumination is investigated and shown to blur the aerial image and increase in severity with depth. This is shown to be a critical limiting parameter in NFNP.

2. Comprehensive Modeling

In the comprehensive modeling framework, separate models were constructed for exposure, post exposure baking (PEB), and developing that each successively operated on a common materials mesh. The exposure model computed irradiance throughout the photoresist, or aerial image, and incorporated diffraction through the phase mask, unpolarized light, line spectrum of source, optical absorption, scattering, and standing wave effects. The PEB model simulated blurring effects of acid diffusion to determine the latent image and accounted for shrinkage due to cross linking. Dissolution rate throughout the photoresist was computed from the latent image using the enhanced notch model [8]. This data was fed into the final model to simulate the developing process.

By combining these models, geometry of formed structures can be predicted more rigorously. Optical performance can be studied more accurately with a higher degree of fidelity. This tool is seen as an enabling step for designing devices that can exploit the physics and compensate for limiting factors inherent in the fabrication process.

2.1 Exposure

Optical absorption, diffraction, coherence, polarization, refraction, scattering, and standing waves are just some effects that must be considered when modeling exposure. Due to the periodic nature of diffraction through a phase grating, rigorous coupled-wave analysis (RCWA) was used instead of finite-difference time-domain (FDTD) from previous work. For grating periods on the order of a wavelength, RCWA runs orders of magnitude faster than FDTD. In addition, RCWA can more efficiently cascade multiple layers (i.e. gratings, air gaps, glass plates, substrates, etc.) of arbitrary thickness because the method obtains an analytical solution in the longitudinal direction.

The code was formulated using conventional RCWA applied to planar grating stacks, but the Fourier expansions were expressed in terms of reciprocal lattice vectors $\vec{g}_1$ and $\vec{g}_2$ of the grating unit cell. This approach improves convergence and formulates the analysis based on wave vectors consistent with grating symmetry. In this framework, the wave vector components of the harmonics were

$$k_{m,n}^{x} = k_{\text{inc}}^{x} + \left(m\vec{g}_1 + n\vec{g}_2\right) \bullet \hat{x} \tag{1}$$

$$k_{m,n}^{y} = k_{\text{inc}}^{y} + \left(m\vec{g}_1 + n\vec{g}_2\right) \bullet \hat{y} \tag{2}$$

$$k_{i,m,n}^{z} = \begin{cases} \sqrt{k_0^2\varepsilon_i - \left(k_{m,n}^{x}\right)^2 - \left(k_{m,n}^{y}\right)^2} & k_0^2\varepsilon_i \geq \left(k_{m,n}^{x}\right)^2 + \left(k_{m,n}^{y}\right)^2 \\ -j\sqrt{\left(k_{m,n}^{x}\right)^2 + \left(k_{m,n}^{y}\right)^2 - k_0^2\varepsilon_i} & k_0^2\varepsilon_i < \left(k_{m,n}^{x}\right)^2 + \left(k_{m,n}^{y}\right)^2 \end{cases} \tag{3}$$

The remaining formulation was consistent with that described in Refs. [9,10].

After simulation, energy absorbed during exposure was computed throughout the photoresist given the absorption coefficient $\alpha(\vec{r})$, irradiance $I(\vec{r})$, and exposure time T.

#7975 - $15.00 USD Received 29 June 2005; revised 1 August 2005; accepted 30 August 2005
(C) 2005 OSA

$$\xi(\vec{r}) = \alpha(\vec{r}) I(\vec{r}) T \,. \tag{4}$$

To model partially coherent sources, simulations at discrete wavelengths were performed and their corresponding irradiances were weighted according to the source spectrum, and summed. This approach has the benefit of modeling sources where multiple or misshaped spectral lines may be present. Unpolarized light was approximated by averaging aerial images resulting from all possible polarizations. When bleaching must be incorporated, absorption evolves throughout exposure [11,12]. RCWA and Eq. (4) must be iterated in small time steps to accurately resolve the bleaching process. This effect is negligible for SU-8 exposed with i-line radiation [13].

2.2 Post Exposure Baking

During the PEB, reaction kinetics and acid diffusion combine to blur the aerial image and form the latent image. It is by this mechanism the effects of standing waves and other quickly varying artifacts are usually eliminated. The process was modeled by convolving the aerial image with a 3D Gaussian point spread function that approximated the diffusion profile of mobile acids.

$$g(r) = \frac{1}{\sqrt{2\pi\rho_{\text{eff}}^2}} \exp\left(-\frac{r^2}{2\rho_{\text{eff}}^2}\right) \tag{5}$$

Parameter r is radial distance from center of diffusion and ρ_{eff} is effective diffusion length. In this work, ρ_{eff} was set to 100 nm from discussion in Ref. [2].

To model shrinkage, mesh resolution parameters were modified according to a shrinkage tensor $\tilde{S}$ using Eq. (6). For most cases, it may be best to assume s_{xx} and s_{yy} are zero since films are usually thin and well adhered to a substrate.

$$\Delta x' = (1 - s_{xx})\Delta x \qquad \Delta y' = (1 - s_{yy})\Delta y \qquad \Delta z' = (1 - s_{zz})\Delta z \tag{6}$$

An empirical equation called the enhanced-notch model was formulated to compute dissolution rate R from concentration of photoactive compound [8]. This equation was modified to compute R directly from energy in the latent image. The new formulation is

$$R(\bar{E}) = R_{\max}(1-\bar{E})^N \left[\frac{(a_n+1)(1-\bar{E})^{N_{\text{notch}}}}{a_n + (1-\bar{E})^{N_{\text{notch}}}}\right] + R_{\min}\left[\frac{R_{\min}^{\bar{E}-1}}{R_{\max}^{\bar{E}-1}}\right]\left[1 - \frac{(a_n+1)(1-\bar{E})^{N_{\text{notch}}}}{a_n + (1-\bar{E})^{N_{\text{notch}}}}\right] \tag{7}$$

$$a_n = \frac{N_{\text{notch}}+1}{N_{\text{notch}}-1}(1-\bar{E}_{\text{th}})^{N_{\text{notch}}} \tag{8}$$

where $\bar{E}$ is a normalized energy parameter in the range $0 \le \bar{E} \le 1$. $R_{\max}$ is the fastest dissolution rate that occurs where no energy is absorbed (i.e., $\bar{E} = 0$). $R_{\min}$ is the slowest dissolution rate in saturated regions (i.e., $\bar{E} = 1$). The parameter $\bar{E}_{\text{th}}$ defines the energy threshold where dissolution rate falls rapidly. Slope of the dissolution rate curve below the notch region is controlled through parameter N. Higher values of N yield steeper slopes. In a similar manner, N_{notch} controls slope in the central region, or notch region, where dissolution rate falls rapidly.

The parameters were estimated experimentally to be $R_{\max} = 7.5 \frac{\mu\text{m}}{\text{sec}}$, $R_{\min} = 5\times10^{-10} \frac{\mu\text{m}}{\text{sec}}$, $\bar{E}_{\text{th}} = 0.51$, $N = 0.8$, and $N_{\text{notch}} = 100$, but these were observed to vary somewhat for different types of SU-8.

#7975 - $15.00 USD Received 29 June 2005; revised 1 August 2005; accepted 30 August 2005
(C) 2005 OSA

2.3 Developing

To simulate the developing process, a fast marching level set method [14] was implemented in place of the cellular automata approach used in previous work. This method computes the time $T(x,y,z)$ when the resist-developer interface passes through each point in a grid. Assuming the dissolution rate $R(x,y,z)$ is only a function of position, the following Eikonal equation must be satisfied.

$$\left|\nabla T(x,y,z)\right| R(x,y,z) = 1 \tag{9}$$

Observing the resist-developer interface may only progress in one direction, an "upwind" scheme can be devised to solve Eq. (9). Time values at grid points along the interface are updated based on time values at grid points on the "upwind", or developer, side of the interface. This was accomplished by expressing Eq. (9) in terms of forward and backward finite-differences.

$$\max^2\left(D_{x-},-D_{x+},0\right)+\max^2\left(D_{y-},-D_{y+},0\right)+\max^2\left(D_{z-},-D_{z+},0\right)=1/R_{i,j,k}^2 \tag{10}$$

$$D_{x-}=\left(T_{i,j,k}-T_{i-1,j,k}\right)/\Delta x \qquad D_{x+}=\left(T_{i+1,j,k}-T_{i,j,k}\right)/\Delta x \tag{11}$$

$$D_{y-}=\left(T_{i,j,k}-T_{i,j-1,k}\right)/\Delta y \qquad D_{y+}=\left(T_{i,j+1,k}-T_{i,j,k}\right)/\Delta y \tag{12}$$

$$D_{z-}=\left(T_{i,j,k}-T_{i,j,k-1}\right)/\Delta z \qquad D_{z+}=\left(T_{i,j,k+1}-T_{i,j,k}\right)/\Delta z \tag{13}$$

The code was initialized by setting all time values upwind of the initial interface to zero, all time values downwind of the initial interface to infinity, and all time values at the initial interface according to Eq. (9). Iteration started at the interface grid point with the smallest time value. The value became fixed and was not modified for the remainder of simulation. Time values at all neighboring grid points were updated in a manner that enforced Eq. (10). Viewing this as a quadratic equation to be solved for $T_{i,j,k}^{\text{new}}$ led to the following formulation to obtain a solution.

$$\left(\frac{T_{i,j,k}^{\text{new}}-m_x}{\Delta x}\right)^2+\left(\frac{T_{i,j,k}^{\text{new}}-m_y}{\Delta y}\right)^2+\left(\frac{T_{i,j,k}^{\text{new}}-m_z}{\Delta z}\right)^2=\frac{1}{R_{i,j,k}^2} \tag{14}$$

$$m_x=\min\left(T_{i-1,j,k},T_{i+1,j,k},T_{i,j,k}^{\text{old}}\right) \tag{15}$$

$$m_y=\min\left(T_{i,j-1,k},T_{i,j+1,k},T_{i,j,k}^{\text{old}}\right) \tag{16}$$

$$m_z=\min\left(T_{i,j,k-1},T_{i,j,k+1},T_{i,j,k}^{\text{old}}\right) \tag{17}$$

After all neighboring time values were updated, iteration continued at whatever grid point currently had the smallest associated time value. This value was fixed and all neighboring grid points were updated. This process continued until time values at all points in the grid were computed and fixed.

For moderate to large problems, the most time consuming task was finding the grid point with the smallest associated time value. To speed simulation, downwind grid points being updated were stored in a min-heap data structure. This is a type of binary tree used to quickly sort and recall the minimum value element. It can be stored in a linear array without the need of data pointers.

After simulation, geometry at any time T_0 during developing was determined by constructing the isometric surface defined by $T(x,y,z)=T_0$. Higher order schemes can be formulated and additional physics can be incorporated using level set methods.

#7975 - $15.00 USD Received 29 June 2005; revised 1 August 2005; accepted 30 August 2005
(C) 2005 OSA

3. Numerical Results

3.1 Comparison with Intensity Threshold Scheme

A photonic crystal may be formed by exposing SU-8 (n=1.67) through a phase grating like that in Fig. 2(a). This grating was designed for operation at 365 nm and can be formed in PMMA using electron beam lithography. Grating period determined the beam angles. Grating pattern and thickness determined the relative power in each beam (diffraction efficiency). To achieve good image contrast, these were adjusted until diffraction efficiency of the dominant modes was approximately balanced. More rigorous optimization would consider image contrast, polarization, or quality of the formed structure itself. The optimized film thickness was found to be 525 nm for near-normal incidence.

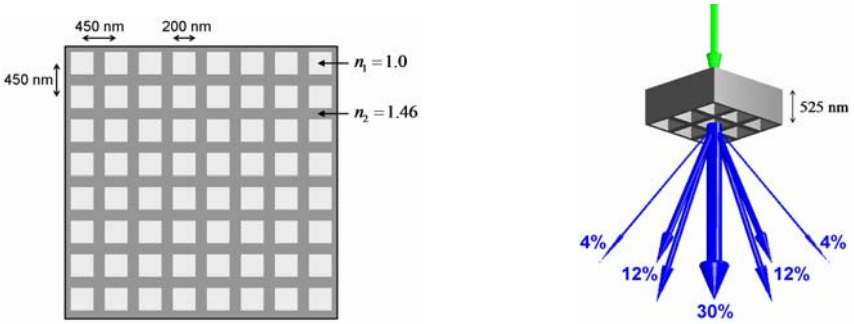

(a) (b)

Fig. 2. (a) Phase grating design. (b) Spectral orders diffracted from grating.

Diffraction through the mask is illustrated in Fig. 2(b) where arrow thickness indicates relative power in the mode. This grating produces five dominant modes, but others exist and must be included for realistic simulation. Reflected modes are not shown in the figure, but were accounted for in simulation.

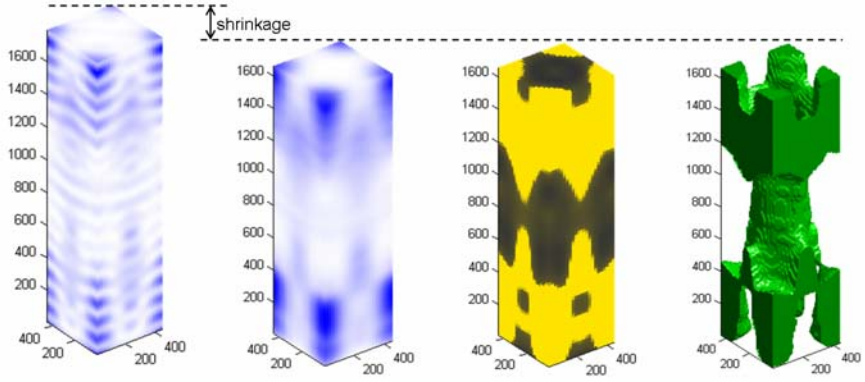

(a) (b) (c) (d)

Fig. 3. Output of comprehensive model at various stages of simulation. Units are in nanometers. (a) Aerial image where blue represents most intense field. (b) Latent image where blue represents most absorbed energy. (c) Dissolution rate where black represents highest solubility. (d) Unit cell of photonic crystal.

Figure 3 shows the output of each stage of the comprehensive model. A standing wave is apparent in Fig. 3(a) suggesting reflections from the fused silica substrate (n=1.52). Acid diffusion during the bake tends to counteract this effect by blurring the aerial image as shown in Fig. 3(b). Vertical dimensions have been reduced by 7.5% due to shrinkage during cross linking [15]. Figure 3(c) shows dissolution rate throughout the photoresist computed from the latent image. Clearly, SU-8 is a very high contrast photoresist leading to few partially soluble

#7975 - $15.00 USD Received 29 June 2005; revised 1 August 2005; accepted 30 August 2005
(C) 2005 OSA

regions. Symmetry appears to be centered-tetragonal. Transmission and reflection spectra from 10 layers of this photonic crystal are shown in Fig. 4(a).

To compare comprehensive modeling to a simple intensity-threshold scheme, irradiance was computed using a scalar sum of the five dominant modes produced by the grating. Intensity-thresholding assumes all portions of photoresist exposed with an irradiance above some threshold will become insoluble and remain intact after developing. A threshold was chosen that produced a photonic crystal with the same fill factor (42%) as comprehensive modeling. Figure 4(b) shows a portion this photonic crystal along with transmission and reflection spectra from 10 layers.

The lattice predicted by intensity-thresholding is not connected at the chosen threshold. Both source polarization and acid diffusion contribute significantly to lattice connectivity. Since these factors are ignored, intensity threshold schemes tend to predict higher fill factor photonic crystals because thresholds must be reduced until lattices are connected. This usually pushes spectral behavior to longer wavelengths. Optical properties can be greatly affected even by subtle error in lattice geometry. For example, the photonic crystal predicted by comprehensive modeling shows a strong band gap in the vicinity of 1550 nm, while the other does not. This indicates more rigorous modeling of fabrication is necessary to accurately predict shape of structures and optical behavior.

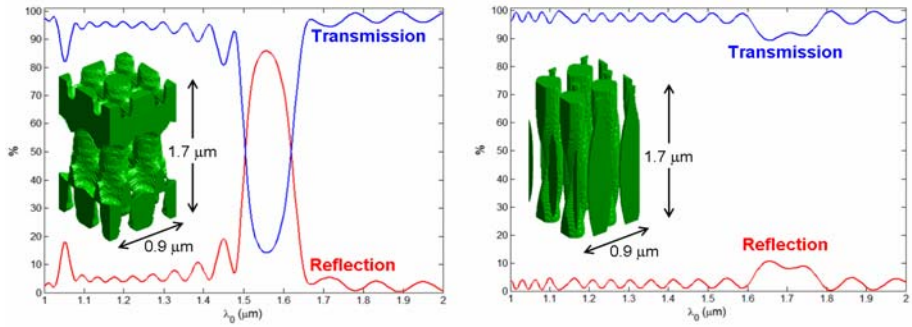

(a) (b)

Fig. 4. Transmission and reflection spectra through 10 layers of photonic crystal. One layer is shown. (a) Comprehensive model. (b) Intensity-threshold model.

3.2 Exposure Using Standard UV Lamps

A very attractive feature of NFNP is that 3D structures can be formed using illumination from standard ultra-violet lamps commonly used in photolithography. These sources typically provide partially coherent light that is "unpolarized." Due to lamps being of finite size, illumination is not purely plane-wave and an angular spectrum must be considered. This is considered in section 3.3.

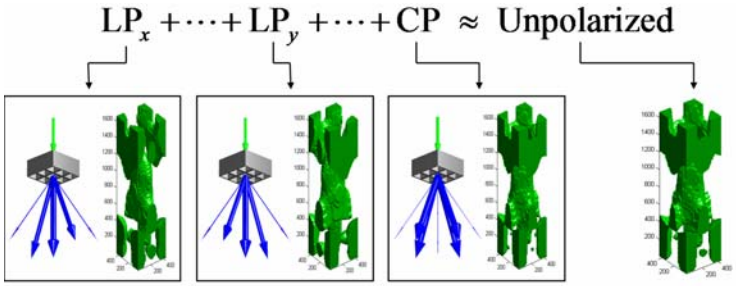

Fig. 5. Approximation of "unpolarized" light source. LP_x represents linear polarization in the x direction. LP_y represents linear polarization in the y direction. CP indicates circular polarization.

#7975 - $15.00 USD Received 29 June 2005; revised 1 August 2005; accepted 30 August 2005
(C) 2005 OSA

Through simulation it was shown that photonic crystals can be formed in the configuration described previously using unpolarized light. This greatly simplifies hardware used for exposure. Figure 5 shows how unpolarized light improved lattice connectivity by effectively summing exposures of different polarizations. For this grating, a linear polarization (LP) alone does not produce a connected lattice, while unpolarized light does.

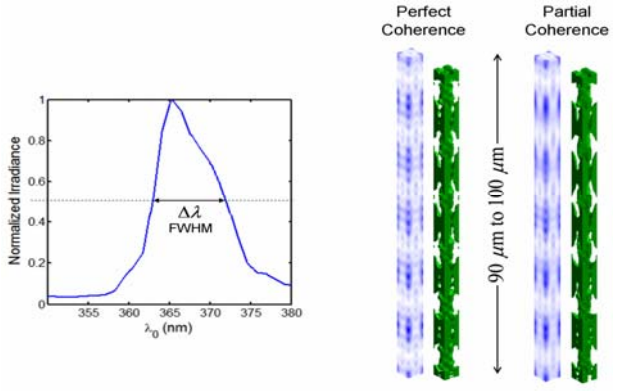

(a) (b)

Fig. 6. Near-field nano-patterning using partially coherent light. (a) Typical i-line profile. (b) Bottom 10 μm of 100 μm film.

Due to dramatically relaxed requirements on beam coherence, 3D structures may be formed using partially coherent light. Figure 6(a) shows the typical i-line spectrum of a mercury vapor lamp. It was assumed a narrowband i-line filter was used to remove additional lines from the spectrum. Figure 6(b) compares aerial images and photonic crystals produced by perfectly coherent and partially coherent light sources. To show useful interference exists far from the grating, the bottom 10 μm of a 100 μm film is depicted in this figure. Partial coherence produces a smoothing effect, but still forms an excellent photonic crystal similar in appearance to the perfectly coherent case. Partial coherence can also contribute to lattice connectivity.

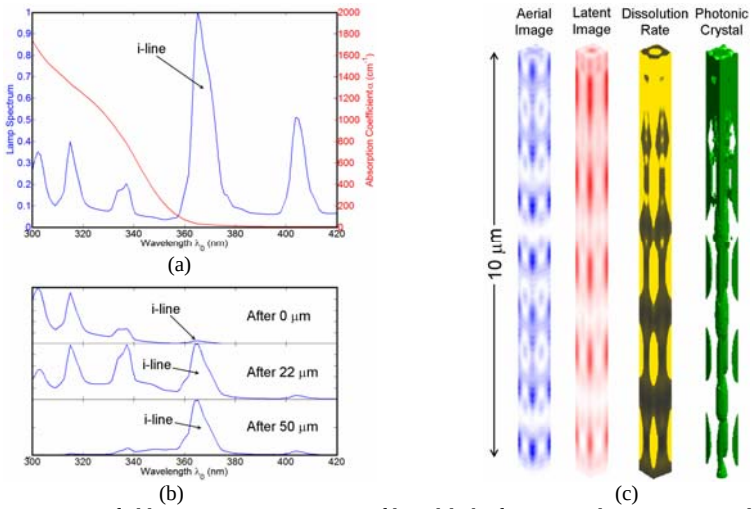

(a) (b) (c)

Fig. 7. Near-field nano-patterning using unfiltered light from typical mercury-vapor lamp. (a) Overlay of lamp spectrum [16] and SU-8 absorption coefficient [13,17]. (b) Normalized weighted lamp spectrum after propagating through different thicknesses of SU-8. Weighted spectrum is defined as the product of absorption coefficient with irradiance. (c) Output of each stage of comprehensive simulation using unfiltered light.

#7975 - $15.00 USD Received 29 June 2005; revised 1 August 2005; accepted 30 August 2005
(C) 2005 OSA

Simulations were performed to explore the effect of using unfiltered light. Figure 7(a) overlays the absorption spectrum of SU-8 against the output spectrum of a typical UV lamp. Despite the i-line being most intense, spectral lines at shorter wavelengths can dominate exposure when absorption is considered. See Eq. (4). To quantify this effect, "weighted" spectra were computed by multiplying source irradiance by the absorption coefficient. These are shown in Fig. 7(b). The uppermost plot clearly shows spectral lines at shorter wavelengths dominate exposure near the surface because they contribute most to absorbed energy there. Irradiance at the shorter wavelengths, however, decays quickly with depth changing the balance of which lines are dominant. At a depth of 22 μm, the spectral lines contribute about equally to absorbed energy. At 50 μm and greater, the i-line dominates exposure.

Figure 7(c) shows the output after each stage of comprehensive simulation for unfiltered light. Bleaching was ignored. The aerial image is a measure of irradiance where the i-line is dominant. The latent image is a measure of absorbed energy where dominance varies with depth. The latent image is shown to differ greatly from the aerial image, especially near the surface of the film where shorter wavelengths dominate exposure. A sharp contrast in solubility can be observed near the surface of the film. The rightmost image in Fig. 7(c) was constructed from isometric surfaces of dissolution rate. The developing model did not show any structure because the top portion of the film was completely insoluble.

The result of using unfiltered light is a region of very high absorbed energy near the surface of the photoresist film. This can lead to the well known "T-topping" or barb-shaped structures that overhang vertical sidewalls. In practice, it would be very difficult to control exposure to form a photonic crystal with unfiltered light. When dose is chosen to form a photonic crystal through most of the volume, the surface of the film would become insoluble and not allow developer to pass through. No photonic crystal would form if dose were lowered to form openings at the surface. With this in mind, it should be possible to form interesting and useful structures by tailoring the relative irradiance of the spectral lines with filters or using photoresist with different absorption properties.

3.3 Angular Spectrum

A critical process parameter to NFNP is the angular spectrum of source illumination. Perfect plane-wave illumination during exposure is ideal, but realistic optical systems suffer from diffraction, scattering, and the penumbra effect where finite size sources produce rays at different angles. Off-axis rays produce tilted aerial images that combine to blur the overall aerial image. Since tilt origin is at the grating, blurring effects increase in severity with distance away from the grating.

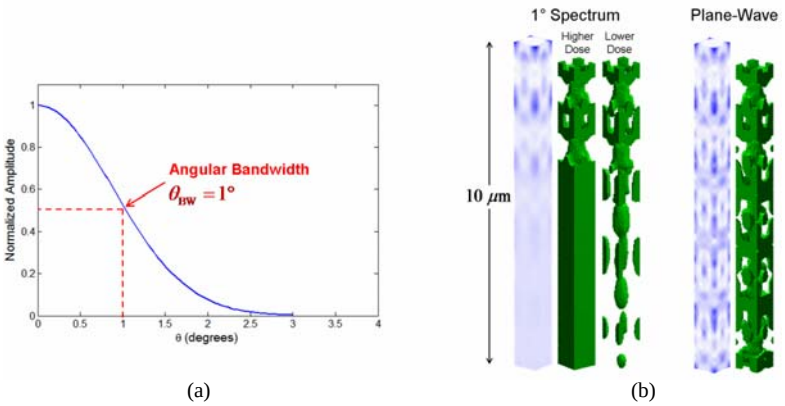

(a) (b)

Fig. 8. Impact of angular spectrum. (a) Assumed angular spectrum. (b) Aerial images and lattices in 10 μm film.

#7975 - $15.00 USD Received 29 June 2005; revised 1 August 2005; accepted 30 August 2005
(C) 2005 OSA

As an example, angular spectrum was incorporated in the configuration described in section 3.1 and results summarized in Fig. 8. The curve in Fig. 8(a) describes the assumed angular dependence of irradiance for an angular bandwidth around 1°. Aerial images and resulting photonic crystals under one grating period are shown in Fig. 8(b). Angular divergence has clearly blurred and "washed out" interference fringes in the aerial image. Within a narrow range of dose, two outcomes were possible. For slightly higher doses, the bottom portion was not soluble and a photonic crystal only formed near the surface. For slightly lower doses, the bottom portion remained soluble and released the photonic crystal from the substrate. When a 5 μm gap was inserted between the grating and photoresist, no crystal formed at all. Under plane-wave illumination, the photonic crystal was virtually uniform with depth. Perhaps this could serve as a mechanism for controlling lattice chirp or compensating for chirp caused by optical absorption during exposure.

Bandwidth of angular divergence should be made small as possible. This is usually a fraction of a degree. A rule-of-thumb can be derived from the geometry of the problem. Given minimum feature size of the resulting crystal $L_{\min}$, refractive index of the photoresist n, and film thickness T, angular bandwidth should be limited to

$$\theta_{\mathrm{BW}} < \frac{nL_{\min}}{T} \tag{18}$$

To illustrate this point, parametric curves were calculated from Eq. (18) and are shown in Fig. 9. The curves show maximum angular bandwidth versus film thickness for five minimum feature sizes. A quality exposure should limit angular bandwidth of the source to angles below the curve. Thicker films and smaller feature size place stricter limits on angular bandwidth.

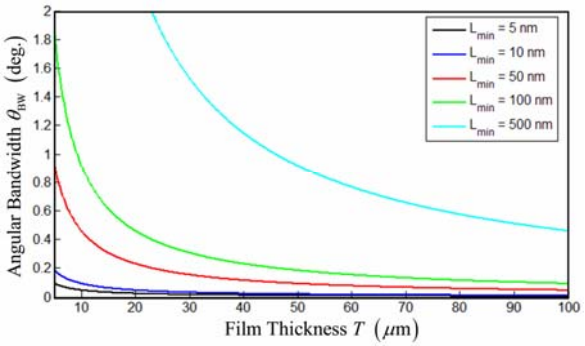

Fig. 9. Parametric curves for limiting angular spectrum. $L_{\min}$ is smallest feature size that must be resolved.

4. Conclusion

Near-field nano-patterning greatly simplifies holographic lithography enabling 3D structures to be formed with less sophisticated equipment. When nano-sized structures are made, physics inherent to fabrication combine to distort shapes of structures from what may be considered ideal. To accurately predict geometry and ultimately optical behavior, all distorting phenomena must be considered.

A fast and efficient comprehensive model of NFNP was described that more rigorously predicts geometry of structures fabricated by this method. Numerical results were presented showing intensity threshold schemes do not adequately predict lattice geometry because most distorting artifacts are ignored. Through simulation, it was demonstrated that 3D structures may be formed using filtered light from standard UV lamps. Angular divergence of source illumination was shown to be a critical limiting parameter. Aerial images were blurred with

#7975 - $15.00 USD Received 29 June 2005; revised 1 August 2005; accepted 30 August 2005
(C) 2005 OSA

increasing severity away from the phase mask. This led to photonic crystals forming only near the surface or released from the substrate altogether.

The comprehensive model described in this paper is a significant improvement on previous work. It is seen as an enabling step in the design of fully optimized three-dimensional nano-structures formed by NFNP. Using this tool, it may be possible to design structures that compensate for, or even exploit, physics inherent in the fabrication process. A similar approach to other fabrication methods may prove equally valuable.

Acknowledgments

This work was funded in part by a career grant from National Science Foundation.

#7975 - $15.00 USD Received 29 June 2005; revised 1 August 2005; accepted 30 August 2005
(C) 2005 OSA

132.170.27.255 {ts '2019-08-29 08:51:57'}